Chapter 4

Joining of C/SiC composite to C103 alloy

In this study, niobium-based alloy C103 is joined to carbon fibre-reinforced SiC (C/SiC) composite utilising commercially available Ticusil® and Cusil® alloy braze filler material. Various characterisation techniques are employed to investigate the interfacial microstructures and evolution mechanism of C/SiC–C103 junctions. Lap shear strength (LSS) is used to evaluate the mechanical performance of the brazed joints. The results show that adding Ti promotes the growth of "nails", a phenomenon favourable for robust joint quality. However, high Ti content deteriorates the bond strength due to the formation of significant brittle intermetallic phases, causing premature delamination of the joints. The response surface methodology (RSM) is employed to examine the interactions among various operating parameters. To attain the high LSS value, the high temperature, inter-mediate reaction time, and low cooling rate are necessary for a Ticusil-based joint, whereas high temperature, low reaction time, and increased cooling rate are preferred for a Cusil-based joint.

4.1 Introduction

The demand for advanced aerospace materials is constantly increasing due to rapid development in the aerospace industry, particularly for advanced reusable launch vehicles and air-breathing hypersonic missiles. These vehicles are propelled by modern turbojet or scramjet engines. The thrust chamber walls of these engines are usually experienced high amounts of stress at elevated temperatures. Disilicide-coated C103, a niobium-based alloy, has extensively been used for the above applications due to its high-temperature and corrosion resistance properties (Awasthi et al. 2022). Since the propellant fuel combustion temperature is typically between 3000 and 3500ºC, a significant portion of the fuel is utilised to cool the thruster to maintain its upper temperature below 1350ºC (Patterson et al. 1996). As a result, it is necessary to develop high-performance materials that can be used at elevated temperatures.

The C/SiC ceramic matrix composites (CMCs) could be attractive materials for advanced rocket propulsion thrust chambers owing to their comparatively low density (1.8–2 g/cc), high mechanical strength (>300 MPa), relatively low coefficient of thermal expansion (CTE), excellent chemical stability, and good oxidation resistance (Rak et al. 2001, Chawla et al. 2003, Jian et al. 2005, Krenkel et al. 2005). If C103 alloy is substituted with a C/SiC material, the trust chamber can be operated up to 1650ºC, thereby increasing the thrust-to-weight ratio (Xiong et al. 2006a, Liu et al. 2004, Schmidt et al. 2004).

A C103-based thrust chamber usually is connected to a less costly Ti alloy-based fuel injector system (Ong et al. 2020). Therefore, substituting C103 alloy and directly joining C/SiC to Ti alloy would be the best choice to form a complete integrated propulsion system. However, excessive Ti dissolution into SiC creates many brittle intermetallics at the interface, resulting in low bond strength (Lia et al. 2022). Therefore, joining C/SiC to C103 would be another alternative because simple welding can integrate the propulsion system with Ti alloy-based fuel injectors.

The joining of C/SiC to metal alloy is frequently challenging owing to the non-wetting nature of C/SiC, the natural development of process-induced microcracks and brittle intermetallics, and the high residual stress at the interface induced by the CTE mismatch between C/SiC and metal (Singh et al. 2007). The various methods for joining C/SiC with metal have been reported in the literature (Singh et al. 2008, Hernandez et al. 2014, Halbig et al. 2015, Fan et al. 2017, Ba et al. 2021, Kumar et al. 2021, Wang et al. 2022). Due to its simplicity, adaptability to different joint sizes and shapes, low processing temperature, and good reproducibility, the brazing technique is the most appealing (Sciti et al. 2001, Liu et al. 2011, Hernandez et al. 2014). The infallible joining of the composite to metal, notably to the Ti-alloys such as TiCu-Cu (Xiong et al. 2007), TiCuAg (Ba et al. 2021, Zhang et al. 2018), TiNi (Tian et al. 2017), TiCuNiZr (Zhang et al. 2018), and TiCoNb (Zhang et al. 2017) using this technology is frequently used in aerospace applications. Adding a Ti metal causes the filler alloy to chemically interact strongly with the C/SiC, forming various intermetallic compounds varying the composition locally. C/SiC composite brazing to Ti alloys using TiCuAg filler with and without adding Ag has been investigated by some researchers (Zhang et al. 2018). A reaction layer comprised of carbide (TiC) is formed at the interface, and the brazed joints are reported to have a shear strength of 102 MPa at room temperature. Yang et al. investigated the microstructure and joint strength of TiAl alloys and C/SiC composite using CuAg and TiCuAg fillers (Yang et al. 2011). Ti and Al atoms dissolve into the C/SiC composite due to the strong reactivity of TiAl, forming an $AlCu_2Ti$ and Ag solid solution. Although the plastic deformation behaviours of CuAg and TiCuAg assisted in reducing the residual stress of joints, they can still be used in low-temperature applications (<800ºC). Therefore, low-expansion materials (W, CuZr alloy), soft metals (Cu, Ni), and high-temperature metals (Mo, Hf) are added into the brazing filler as the reinforcing phase so that the CTE mismatch between filler and the composite is minimised and that joint can be used at high temperature. Another advantage of adding these materials is that they control the excessive Ti dissolution into the C/SiC and minimise the formation of brittle phases (Xiong et al. 2006a, Lia et al. 2022). Cui et al. used (Ti–Zr–Cu–Ni)+W mixed powders as fillers to join the C/SiC composite to the TC4 alloy. They discovered that adding the right amount of tungsten powder is advantageous to reduce residual thermal stress. The maximum shear strength of 166 MPa and 96 MPa was achieved at room temperature and 800ºC, respectively (Cui et al. 2014). Another work used Ti–Zr–Be filler to actively braze C/SiC composite to 304 stainless steel (Fan et al. 2014). The results showed that the Ti, Be diffused into 304 stainless steel and formed a variety of intermetallics, including TiBe, Ti_5Si_3, TiFe, Zr(s,s) and TiSi. At 950ºC, the maximum shear strength of 109 MPa is attained. Besides, TiNi and TiCoNb-based fillers were also utilised to investigate the strength of the C/SiC–Nb joint at high temperatures (Tian et al. 2017, Zhang et al. 2017). They presented the laser drilling holes on the C/SiC surface to improve brazing characteristics. Ba et al. proposed an optimised root-like structure on the C/SiC surface through selective electrochemical corrosion to redistribute the residual stresses when brazed to Nb. They observed a 92% increase in the shear strength of the joints (164.3 MPa) compared to the original joints (Ba et al. 2021). To decrease the residual stress of C/SiC-metal junctions, researchers recently have proposed a unique brazing alloy composition by adding negative thermal expansion materials such as ZrP_2WO_{12}, $Y_2Mo_3O_{12}$ and $Sc_2W_3O_{12}$ to the braze alloy (Ba et al. 2019, Wang et al. 2022, Wang et al. 2023). A careful examination of the literature revealed that the microstructural development of C/SiC composites and C103 alloys, crucial for aerospace applications, has not been reported yet. Vacuum brazing C/SiC composites and C103 alloys with highly active Ticusil® and less active Cusil® fillers are therefore used in this study.

The brazing process parameters significantly impact the interfacial interaction between the C/SiC composite and joining material, ultimately deciding the mechanical strength of the joint. For instance, more Ti dissolves into the C/SiC substrate as the brazing temperature and reaction time increase, and the extent of interfacial reactivity of Ti with the composite also increases. As a result, pores emerge in the brazing layers (Lia et al. 2022). Therefore, optimising various process parameters, including brazing filler composition, temperature, reaction time, and heating-cooling rates, is essential to obtain the high strength of the joint. Response surface methodology (RSM), a mathematical-statistical tool, is employed in this context to examine the interaction effect of different experimental factors (input variables) on the objective function (response function) and to predict the optimum experimental conditions. The process optimisation of joining the niobium alloy (C103) to the C/SiC composite has not been reported yet in the literature. Therefore, the present work investigates the interfacial evolution mechanism and microstructure of brazed C/SiC composite and C103 alloy using commercially available Ticusil (highly active) and Cusil (less active) fillers. By assessing the lap shear strength (LSS), the effect of the Ti content and the process parameters on the joint quality is determined. To determine the high LSS value, the RSM is employed to predict the optimum process variables.

4.2 Experimental

4.2.1 Fabrication of joints

The composite was prepared using carbon fabric (T-300, 3K, 8H, Toray Japan) as reinforcement material. 2.5D carbon fabric preform was prepared by stitching fabric plies of the desired sizes. The pyrolytic carbon (PyC) interface of ~1 μm thickness was then created on the carbon fabric preform in a chemical vapour infiltration (CVI) reactor (Fig. 4.1). The SiC matrix was then infiltrated through the thermal cracking of 8% (volume basis) methyl trichlorosilane at 1100ºC and 80 mbar pressure with hydrogen as the carrier gas. The densification process was carried out in multiple cycles until the desired density (1.9–2.0 g/cc) was achieved. Thus obtained C/SiC composite (density: 2.0 g/cc, fibre: ~35 vol %, porosity: 12–15%, flexural strength: 350–380 MPa, interlaminar shear strength: 20–22 MPa) was machined into desired coupon sizes for brazing experiments. XRD analysis of composite material prepared by the CVI technique confirms the presence of the β-SiC matrix. The optical image of C/SiC composite is presented in Fig. 4.2. The microstructure of C/SiC composite and C103 alloy is displayed in Fig. 4.3. Arrow marks denote the transverse, longitudinal, and stitched fibres of the composite in the figure. The presence of inter-bundle pores and the fibre bundles covered with the β-SiC matrix can also be observed.

Two different types of filler, namely Ticusil® and Cusil® alloys of 100 μm thickness each, were used as the brazing material. The brazing alloys and C103 alloy were procured from

Maxon Engineering Technology, Bengaluru and M/s. Kalapurna Steel and Engineering Pvt. Ltd., Mumbai, respectively. The physicochemical properties of all three alloys are given in Table 4.1. The joining surfaces of C103 alloy and C/SiC composite were machined and polished using SiC emery paper (320 grit size). Before the brazing experiment, all specimens were ultrasonically cleaned in isopropyl alcohol for 15 min and then dried at 150ºC in an air oven.

Fig. 4.1: Chemical vapour infiltration (CVI) reactor in VSSC/ISRO.

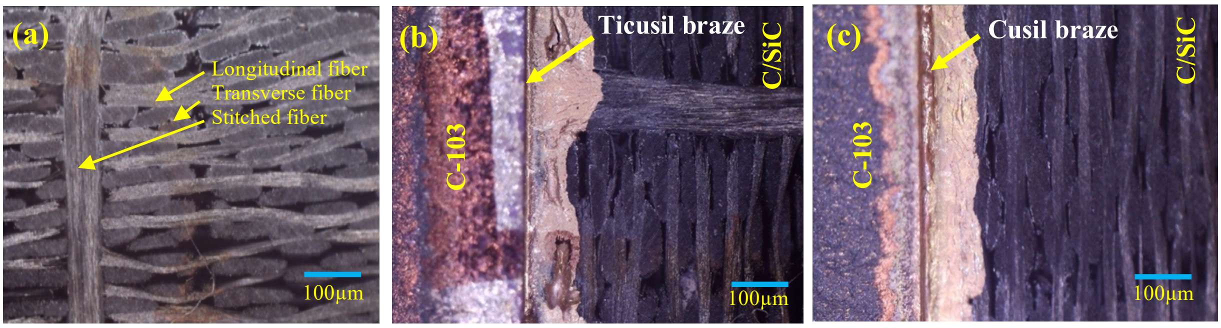

Fig. 4.2: Optical image of (a) C/SiC, (b) Ticusil-based, and (c) Cusil-based C/SiC-C103 joint.

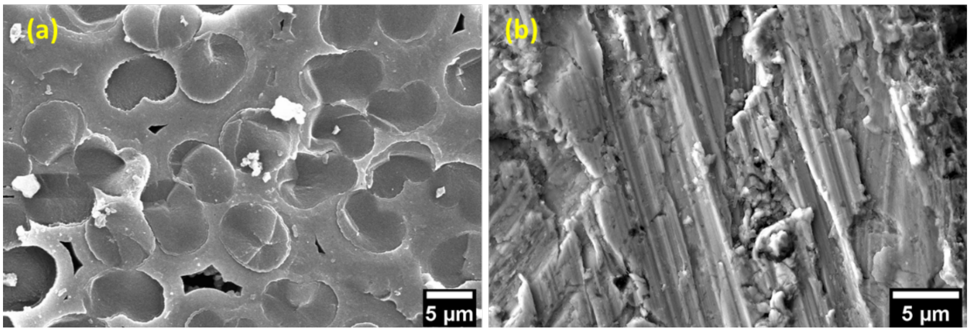

Fig. 4.3: SEM micrographs of (a) C/SiC composite and (b) C103 alloy

The differential scanning calorimetry (DSC) analysis of Ticusil and Cusil brazing foils revealed that the melting point of both foils was in the range of 787–790ºC (Fig. 4.4).

Therefore, the minimum brazing temperature was selected as 800ºC (above the melting point of brazing foils) to ensure sufficient liquidity of the foil. The brazing furnace (Fig. 4.5) was maintained at a vacuum level of 10^{-3} mbar, and a dead load of 0.25 kg/cm^2 was applied to ensure good contact between the braze and substrate. The optical images of the interface of post-brazed C/SiC–C103 joints are depicted in Fig. 4.2. The good melting and ooze out from the edges (marked by arrows in Fig. 4.2b and c) confirmed excellent wetting of the C/SiC substrate and metal surface by the brazing alloys (Naidich et al. 2008).

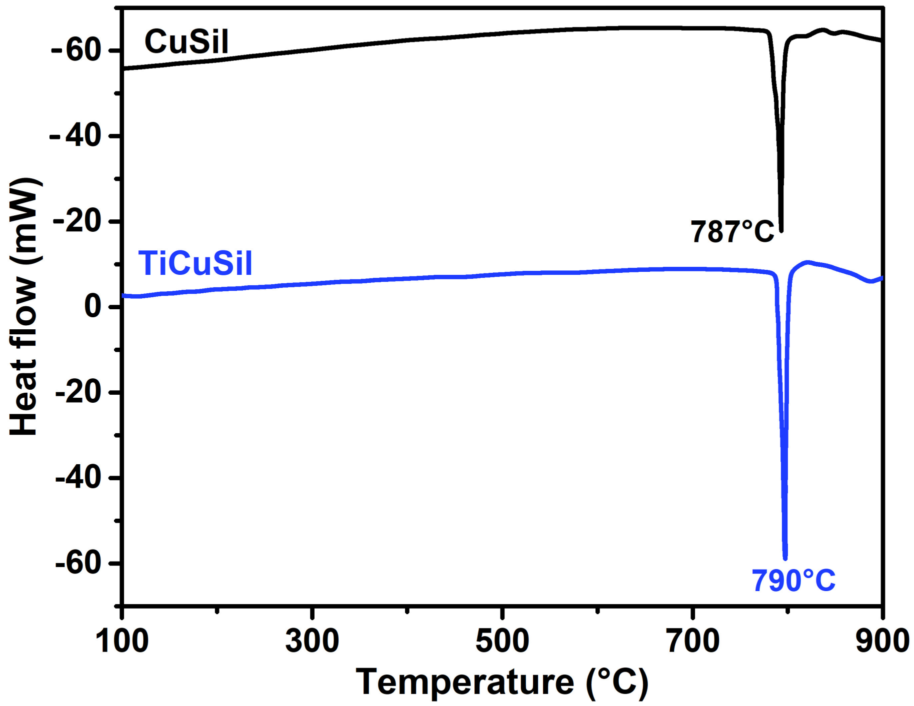

Fig. 4.4: DSC curves of Ticusil and Cusil braze alloys.

Fig. 4.5: Vacuum brazing furnace.

Table 4.1: Physicochemical properties of the alloys

Properties	Unit	Ticusil	Cusil	C103
Chemical composition				
Ti	Wt.%	4.5	1.75	0.0
Cu	Wt.%	26.7	35.25	0.0
Ag	Wt.%	68.8	63	0.0
Nb	Wt.%	0.0	0.0	89
Hf	Wt.%	0.0	0.0	10
Zr	Wt.%	0.0	0.0	1
Physical Properties				
Density	g/cc	9.4	9.8	8.85
Yield Strength	MPa	290	275	400
Young's modulus	GPa	85	83	85
CTE	$\times10^{-6}$/K	18.5	18.5	17.3
Melting point	°C	790	787	-

4.2.2 Microstructural characterisation

The DSC analysis was performed at a heating rate of 10ºC/min in an argon environment. The samples were mounted in transparent epoxy upto 140°C. Hot press epoxy mounted samples were polished to 1 µm grit finish using Carbimet cloth, Texmet C cloth, micro-cloth, micro-polishing suspension, and alumina suspension for the investigation of the microstructure of the joint interface. The joint interlayer and fracture surface microstructure were examined using a scanning electron microscope (SEM) (Make: Zeiss, Model: Supra 55) with a 15 kV accelerating voltage. The elemental composition of specimens was analysed by an energy dispersive spectrometer (EDS) (Make: Bruker, Model: X Flash 6160). Phase characterisation was performed using an XRD instrument (Philips) by directing an X-ray beam at the sample through Cu-Kα radiation (λ=1.5418 Å). The spectra were recorded at 25ºC with the step size and the time per step of 0.02º and 0.5 s, respectively. An optical profilometer was implemented to reconstruct the 3D image by moving the piezo drive on fracture surfaces of the C/SiC–C103 joint.

4.2.3 Evaluation of LSS

LSS was evaluated using the universal tensile testing machine with a lap area of 10 mm × 10 mm. The schematics for the LSS evaluation set-up and specimen configuration are depicted in Fig. 4.6. A crosshead speed of 0.5 mm/min was maintained throughout the LSS test until the specimens were fractured. Three samples were evaluated for each bonding experiment, and the average value was reported.

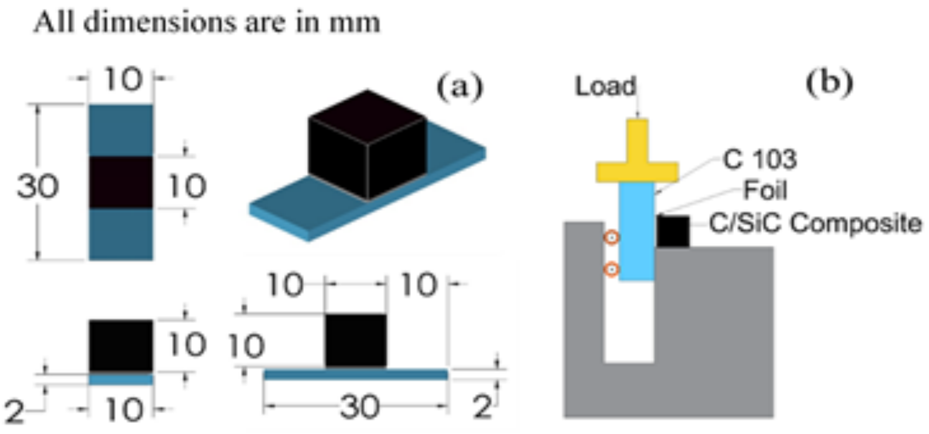

Fig. 4.6: (a) C/SiC-C103 test specimen configuration and (b) LSS test set-up.

4.2.4 Response Surface Methodology

The process parameters such as temperature, time, and cooling rate significantly influence brazed joint strength (Xiong et al. 2006a, Singh et al. 2008, Liu et al. 2011, Zhang et al. 2017, Zhang et al. 2018, Ba et al. 2021). Response surface methodology (RSM), a conjunction of mathematical and statistical techniques, helps explore a functional relationship between the response (LSS) and the independent process variables (Myers et al. 2004, Khuri et al. 2010). The basic idea of this technique is to approximate the response variable by an explicit function of the process parameters (random variables) and understand the interactions among them. Central composite design (CCD) was exercised to determine the total experimental runs required to obtain the process response using various combinations of the above-mentioned independent variables. The levels of process parameters and their experimental design levels are presented in Table 4.2.

Table 4.2: Process variables with their experimental design levels

Process Variable	**Notation**	**Unit**	**Levels**		
			-1	**0**	**+1**
Temperature	T	°C	800	820	840
Time	t	min	10	35	60
Cooling Rate	CR	°C/min	1	3	5

Table 4.3: CCD matrix with actual independent process variables and responses

Exp. No.	**Run order**	**Space Type**	**Actual variables**			**LSS (MPa)**	
			°C	**min**	**°C/min**	**Ticusil**	**Cusil**
1	14	Axial	820	35	5	10.2	11
2	6	Factorial	840	10	5	8.4	16.5
3	7	Factorial	800	60	5	0.8	8.2
4	18	Center	820	35	3	10.2	8.7
5	5	Factorial	800	10	5	2.5	13
6	11	Axial	820	10	3	10	11
7	8	Factorial	840	60	5	7.7	7.7
8	12	Axial	820	60	3	10	9.5
9	1	Factorial	800	10	1	5.9	8
10	9	Axial	800	35	3	4	8.3
11	15	Center	820	35	3	10.7	8.4
12	16	Center	820	35	3	10.1	7.8
13	3	Factorial	800	60	1	4.1	13.9
14	2	Factorial	840	10	1	10.2	10
15	4	Factorial	840	60	1	10	13.8
16	19	Center	820	35	3	9.7	8.8
17	10	Axial	840	35	3	8.8	8.4
18	13	Axial	820	35	1	13.7	12.8
19	17	Center	820	35	3	10.3	8.9
20	20	Center	820	35	3	10.2	8.8

The range of the variables was selected based on the hardware limitations of the experiment facility. Twenty experimental runs suggested by CCD are summarised in Table 4.3. The LSS was measured for each experiment of Ticusil and Cusil-based joints, and the values are given in Table 4.3. The interactions among input variables were examined using Design-Expert, a statistical software based on the principle of the analysis of variance (ANOVA). A second-order polynomial response surface model was fitted to examine the impact of the process-independent variables.

$$y=\beta_0+\sum_{i=1}^{k}\beta_i x_i+\sum_{i=1}^{k}\beta_{ii}x_i^2+\sum_{i<j}^{k}\beta_{ij}x_i x_j+\varepsilon \tag{4.1}$$

In the above equation, y is the respective predicted LSS and x_i are the values of the i^th^ coded brazing independent variables. The terms β_i, β_{ii}, and β_{ij} are the regression coefficients, and the residual ε denotes the error during the experimental observations.

4.2.5 Objective function

The mathematical function, Eq. (4.1), was utilised to explore the combination of process parameters (independent variables), maximising the LSS. To this end, the obtained response, y, was transformed in terms of the desirability function (between 0 and 1). This transforms the estimated response (LSS) to the desirability function, which can be represented as:

$$d=\begin{cases}0 & \hat{y}\le y_{low}\\ \left(\dfrac{\hat{y}-y_{low}}{y_{high}-\hat{y}}\right)^{w} & y_{low}\le \hat{y}\le y_{high}\\ 1 & \hat{y}\ge y_{high}\end{cases} \tag{4.2}$$

Where d denoted the desirability of the LSS and was assigned to the target with corresponding high values during the optimisation process. w is the weighted factor for the LSS response that governs the shape of function d. Thus, the objective function illustrated in Eq. (4.2) was maximised with the constraints given in Table 4.2.

4.3 Results and Discussion

4.3.1 Joint microstructures and composition

Fig. 4.7 displays the SEM-EDS images of the interphase of the Ticusil-based joint. The melt is well dispersed throughout the inter- and intra-bundle pores of the composite, as can be seen in Fig. 4.2. As a result, a uniform and continuous joint was formed without interfacial microvoids and cracks. The joint interfaces reveal an interaction zone of ~1–3 μm thick. At a few locations (Fig. 4.7a), extended diffusion of braze constituents into the C/SiC composite was seen; these regions are commonly referred to as "nails" (Xiong et al. 2006a). These "nails" can be categorised into two types, namely long nails (>5 μm) and short nails (< 5 μm). In the instance of Ticusil-based joints, both types of nails were *in-situ* produced.

The EDS composition analysis and possible phases near the interface for Ticusil-based joints are summarised in Table 4.4. The elemental compositions presented in the table correspond to the relative atomic percentages of the elements at the various points marked in Fig. 4.7a. EDS mapping analyses in Ticusil-based joints are also shown in Fig. 4.7 to demonstrate the distributions of the elements at the interface.

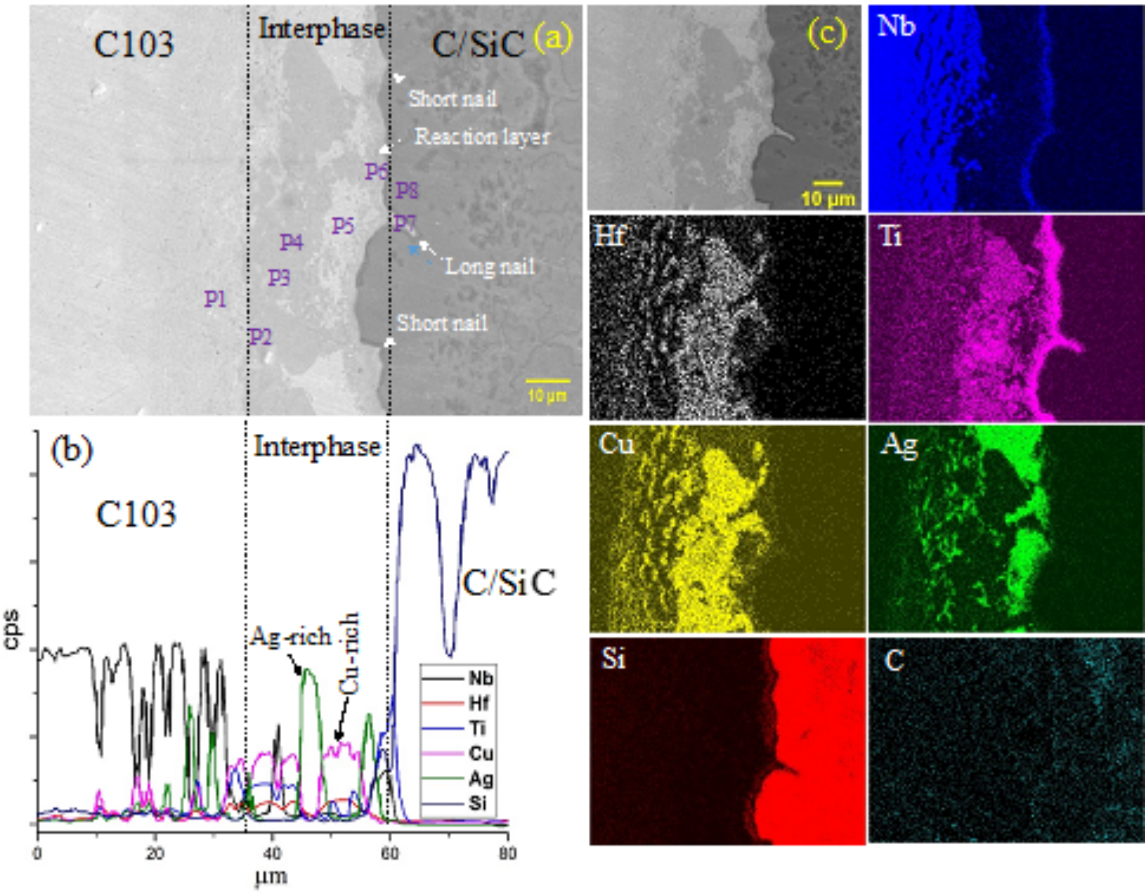

Fig. 4.7: (a) SEM image, (b) line scan, and (c) elemental mapping of the cross-section of Ticusil-based joint.

The composition at point P1 is similar to the metal substrate. Point P2 primarily consists of TiC and Cu (s,s) phases. The presence of TiC in this region can be attributed to the possible reaction of Ti with C/SiC (reaction 4.3). The TiC phase is known to encourage the production of solid-solution Cu (s,s), which increases the high-temperature resilience of the joint (Subramanian et al. 1994, Yang et al. 2013, Wang et al. 2021). Moreover, the element Nb from C103 can diffuse and react with the carbon, forming Nb_2C at point P3 according to reaction 4.4 (Liu et al. 2011, Wang et al. 2022a, Wang et al. 2022b). Additionally, the separation of Cu and Ag phases was observed, forming Cu-rich and Ag-rich at point P4 and point P5, respectively. The formation of these phases is consistent with the Cu–Ag phase diagram. At below the eutectic point, the limited solubility of Ag in Cu and vice versa causes precipitations of these phases during the cooling process (Kawecki et al. 2012). Similar Cu–Ag solidification segregation was observed by Liu et al. while studying the brazing of SiC monoliths using CuAg-based filler (Liu et al. 2009).

Table 4.4: Elemental composition and possible phases for Ticusil-based C/SiC–C103 joint

Location	**Composition (at.%)**							**Possible phases**
	Nb	**Hf**	**Ti**	**Cu**	**Ag**	**Si**	**C**	
P1	88.00	8.89	2.68	0.00	0.00	0.00	0.43	Nb (s,s)
P2	1.62	0.57	21.95	42.34	0.65	0.00	32.88	TiC, Cu (s,s)
P3	32.6	0.00	5.57	5.37	2.84	1.07	52.55	Nb_2C, TiC
P4	13.55	0.63	23.82	29.48	0.70	19.04	12.78	TiC, Nb_2C, Ti_5Si_3, Cu (s,s)
P5	1.67	0.00	1.17	5.42	67.42	1.38	22.95	Ag rich
P6	9.03	0.46	27.89	3.14	0.82	12.05	46.60	TiC, Nb_2C, Ti_5Si_3
P7	0.88	0.00	9.51	0.59	0.18	39.80	49.04	SiC, TiC
P8	0.34	0.00	0.00	0.00	0.00	43.64	56.02	SiC

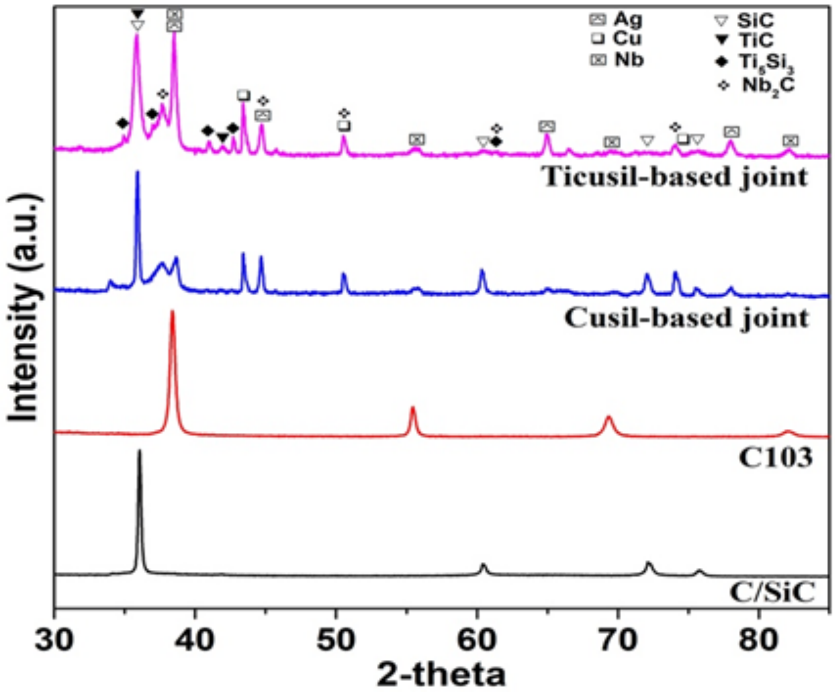

Fig. 4.8: XRD patterns of substrates and C/SiC-C103 joints.

Point P6 is mainly composed of TiC, Nb_2C and Ti_5Si_3 phases that are formed according to reactions (4.3)–(4.7) (Xiong et al. 2006a, Wang et al. 2021, Wang et al. 2022a, Wang et al. 2022b). The elemental mapping at point P7 indicates that this area predominantly comprises the TiC phase (long "nails"), formed due to the reaction between SiC and Ti, as described in reaction 4.8. Elemental analysis at point P8 is very similar to the C/SiC substrate. The interfacial reaction zone (IRZ) at the interface has a thickness of about 3 μm. The IRZ is enriched in Ti, as evidenced by the line scan and EDS results. Likewise, low silicon concentration is also observed in this region. At the brazing temperature, it appears that Ti quickly diffuses and reacts with carbon from the C/SiC substrate to form the stoichiometric titanium carbide and various non-stoichiometric carbides. Therefore, the separation of Ti and C at the interface is caused by the high chemical reactivity of Ti towards C, facilitating the wetting and bonding of the Ticusil-based joint. In addition, Nb has also a high affinity for C, forming niobium carbides (reactions 4.4 and 4.7). In contrast to Ti, which is already present at the interphase, Nb atoms diffuse far from the C103 alloy to C/SiC and react with C to aid in forming the thinner Nb-containing layer in IRZ (see Fig. 4.7c).

$$Ti + C \rightarrow TiC \tag{4.3}$$

$$2Nb + C \rightarrow Nb_2C \tag{4.4}$$

$$5Ti + 3SiC \rightarrow Ti_5Si_3 + 3C \tag{4.5}$$

$$5Ti + 3Si \rightarrow Ti_5Si_3 \tag{4.6}$$

$$Nb + C \rightarrow NbC \tag{4.7}$$

$$Ti + SiC \rightarrow TiC + Si \tag{4.8}$$

Gibbs free energy for forming TiC, Nb_2C and Ti_5Si_3 are negative, suggesting that these phases are possible during brazing (Liu et al. 2009, Yang et al. 2017). The free energy for the formation of TiC and SiC in the temperature range 828–840ºC is about − 170 kJ/mol and − 45 kJ/mol, respectively. This indicates that the TiC phase is more thermodynamically stable than the SiC. Therefore, the Ti is expected to react with SiC at the interface to form a stable TiC phase (reaction 4.8), releasing free Si (Yang et al. 2017). Subsequently, the Si can react with excess Ti and form various Ti-containing intermediate phases (e.g., Ti_5Si_3 and $TiSi_2$). The Ti_5Si_3 phase, due to its lower Gibbs free energy (~175 kJ/mol), dominates the formation of $TiSi_2$ (reactions 4.5 and 4.6) (Yushin et al. 2005, Shi et al. 2018, Ba et al. 2019). Besides, the formation of Nb_2C (reaction 4.4) is thermodynamically favoured over NbC (reaction 4.7), as reported elsewhere (Wang et al. 2022b). The formation of stable phases such as TiC, Nb_2C, and Ti_5Si_3 by the reaction of the constituents of Ticusil braze with the substrates is also confirmed by XRD, as presented in Fig. 4.8. The titanium carbide layer may grow close to the C/SiC interface, and subsequently Si may diffuse through it and interact with Ti to form titanium silicides (Singh et al. 2012).

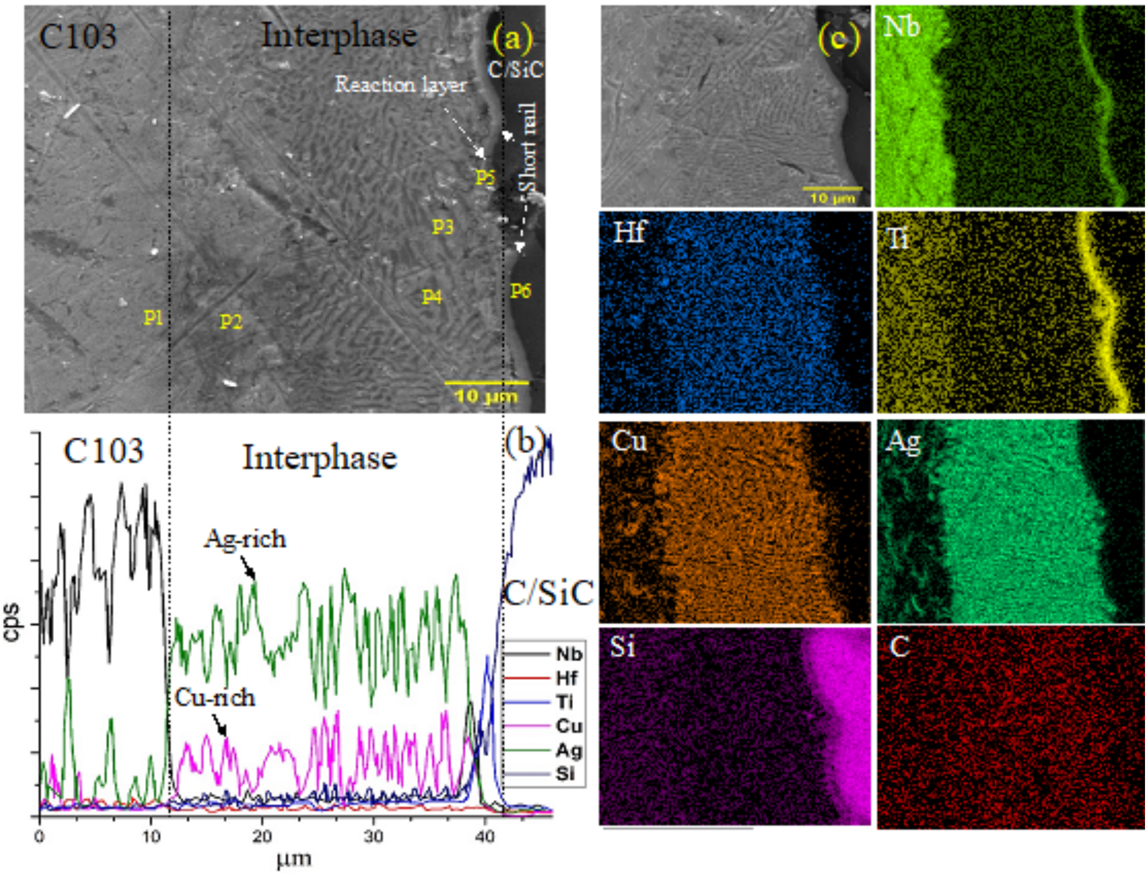

Fig. 4.9: (a) SEM image, (b) line scan, and (c) elemental mapping of the cross-section of Cusil-based joint.

An optical image of the Cusil-based C/SiC–C103 joint is shown in Fig. 4.2c. It can be seen that the initial interlayer thickness of 100 µm is reduced to ~30 µm due to the rapid diffusion of constituent elements of filler and their reactions with the C/ SiC substrate during the brazing process. Additionally, some molten braze is wasted due to the ooze out from the edges. No voids, cracks, or pores were observed at the interface, indicating a robust joint similar to Ticusil-based. The EDS micrographs of the Cusil-based interface, as shown in Fig. 4.9, suggest that a significant diffusion of the melted foil occurred during the brazing process. The IRZ thickness is much smaller (~1 µm) compared to Ticusil-based joints (~3 µm) due to the lesser Ti content of the former. Similar to the Ticusil-based joint, the Nb-containing layer (Fig. 4.9c) is formed at the IRZ of the Cusil-based joint, however, the layer is relatively thinner than the Ti-containing layer in agreement with our earlier explanations. Since Ti has a very high affinity toward C, high Ti contents of Ticusil-based joints facilitate longer diffusion paths and develop large "nails" compared to the Cusil-based joint (Singh et al. 2008). It is known that the large IRZ near the substrate is liable to generate cracks due to high residual stress concentration (Wang et al. 2022b). Therefore, a relatively thin IRZ, as evidenced by line scan and EDS mapping, can be attributed to the low Ti content of the Cusil-based joint. The results of the EDS analysis, as marked at points P1–P6 in Fig. 4.9, are summarised in Table 4.5.

Table 4.5: Elemental composition and possible phases for the Cusil-based C/SiC-C103 joint

Location	Composition (at.%)							Possible phases
	Nb	Hf	Ti	Cu	Ag	Si	C	
P1	87.58	9.58	1.21	0.15	0.00	0.00	1.63	Nb (s,s)
P2	32.6	0.00	5.57	5.37	2.84	1.07	52.55	Nb_2C, TiC
P3	15.58	0.10	1.05	55.65	12.65	0.55	14.42	Cu rich
P4	12.10	3.55	1.10	9.05	60.54	1.11	12.55	Ag rich
P5	4.02	3.78	7.25	4.50	2.46	22.34	55.65	Nb_2C, TiC, Ti_5Si_3, SiC
P6	0.45	0.16	0.13	0.18	0.00	37.57	61.51	SiC

The composition at points P1 and P6 corresponds to the C103 and C/SiC substrates, respectively. The composition at P2 indicates the presence of TiC and Nb_2C as primary phases formed according to reactions (4.3), (4.4), and (4.8). Cu and Ag-rich phases segregate at points P3 and P4, respectively, similar to the Ticusil-based joint. Point P5 signifies the reaction layer composed of Nb_2C, TiC, Ti_5Si_3, and SiC. XRD pattern of Cusil-based joints is also presented in Fig. 4.8. The formation of a relatively lesser amount of Nb_2C, TiC, and Ti_5Si_3 phases is observed in the case of Cusil-based joints.

4.3.2 Fracture surface analysis

The SEM images and elemental mapping of the fracture surface of the Ticusil-based joint are depicted in Fig. 4.10. The three visually distinct regions, namely the bonded layer, bright white, and dark grey regions, are also observed at the interface. The bright white patch region is circular and elemental mapping suggests it is primarily composed of the TiC phase. This structure is formed due to the protrusion of carbon fibre bundles perpendicular to the interface. It has the advantage of enhancing the interfacial bond strength as the protrusion of carbon fibre reinforces the structure and provides an additional anchoring effect (Fan et al. 2017). Besides, the dark grey region is characterised as a SiC phase. It can also be seen that a small fraction of the C/SiC composite layer is attached to the C103 substrate, and tiny “nails” are noticed on top of it. EDS analysis suggests that this structure primarily consists of a TiC phase that might be grown due to the extended diffusion of Ti into the C/SiC composite pores. As discussed earlier, ‘TiC nail’ promoted good wetting and bonding; consequently, the C/SiC layer remained attached to the C103 alloy during LSS evaluation.

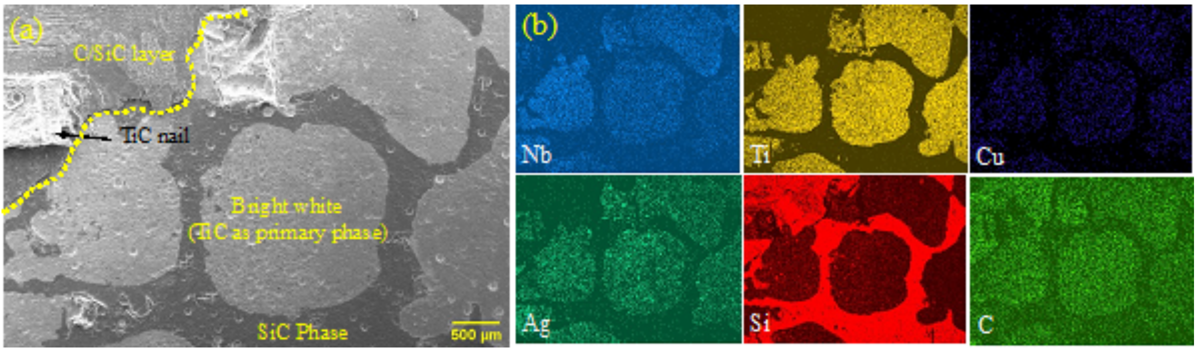

Fig. 4.10: (a) SEM image and (b) elemental mapping of fracture surface of Ticusil-based joint.

According to SEM images, the C/SiC substrate next to the C103 is where the fracture primarily occurred. The CTE mismatch between the substrates and the brazing products (reacted and unreacted) is responsible for the concentration of residual stresses in that region (Bartlett et al. 1991, Lee et al. 1997). Thus, the cracks develop due to the relaxation of residual stresses during loading and propagate through the composite layer, leading to premature failure of the joint. In summary, the bonding of C/SiC to C103 using Ticusil is strong; however high reactivity of Ti with the C fibre and SiC matrix of C/SiC deteriorated the integrity of the C/SiC layer, and the entire bond potential could not be utilised.

The SEM image and elemental mapping for the fracture surface of the Cusil-based joint are also presented in Fig. 4.11. A couple of distinct regions, namely the C/SiC bonded layer (a yellow dotted line) and grey regions, are observed. The bright white region, as seen in the Ticusil-based joint, is not present. In addition, more uniform and homogeneous joint structures are obtained due to the less Ti content of the Cusil-based joint. Notably, a relatively significant fraction of the composite layer is attached to the C103 substrate compared to the Ticusil-based joint, indicating that the bond between the C/SiC and C103 is stronger than the Ticusil-based joint. Thus, forming a small amount of brittle phase (e.g., TiC, Nb_2C, and Ti_5Si_3) is responsible for the increased bond strength of the Cusil-based joint. While the Ticusil-based joint showed a relatively higher amount of TiC, Nb_2C, and Ti_5Si_3 as newly formed phases, EDS analysis of the grey phase region indicates the presence of Ag, Cu, Nb, and Hf (from C103 alloy) with minimal TiC.

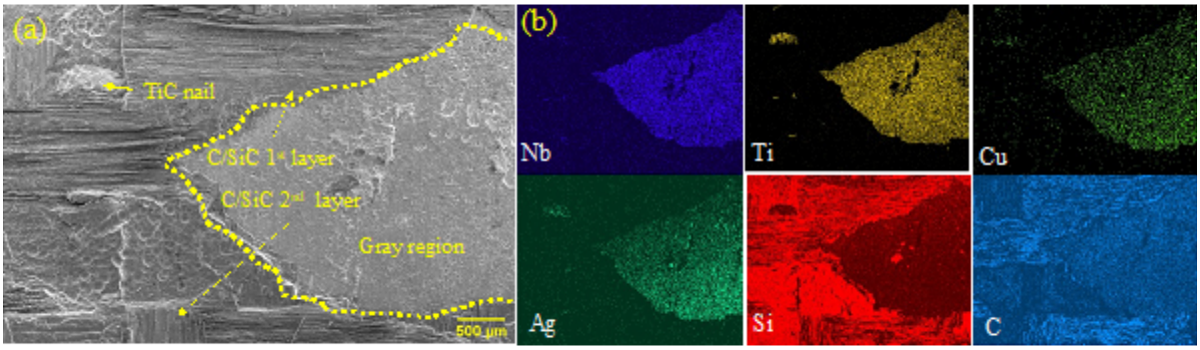

Fig. 4.11: (a) SEM image and (b) elemental mapping of fracture surface of Cusil-based joint.

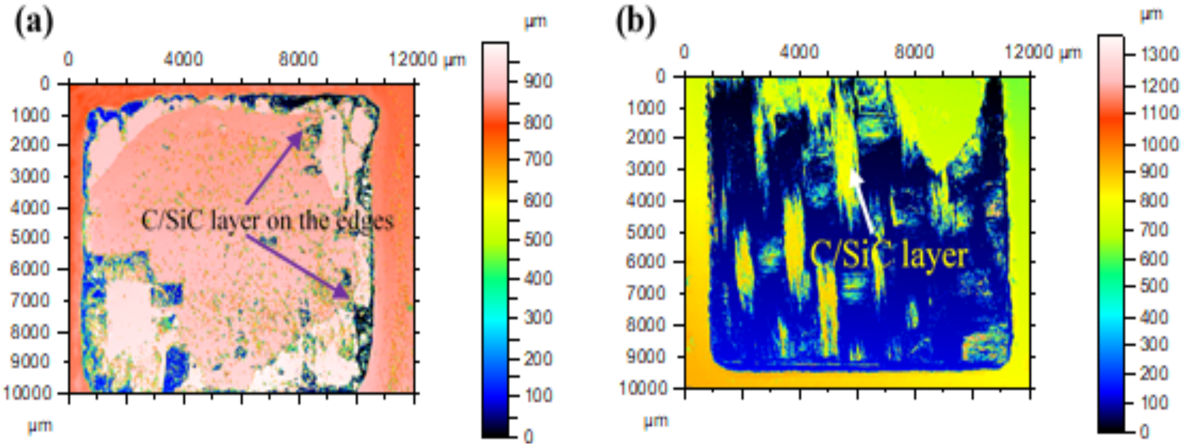

Fig. 4.12: Optical profilometer image of the fracture surface of (a) Ticusil and (b) Cusil-based joints.

The optical profilometer images of the fracture surface for both joints are also presented in Fig. 4.12. The morphology of the fracture surface reveals the presence of a braze joint and C/SiC substrate. The joint covered a larger area of the fractured surface, and C/SiC is primarily present on the edges, confirming that the fracture of the specimen is due to brittle failure mode. Interestingly, the crack propagation is along the joining interlayer, resulting in delamination at the outermost layer of the C/SiC composite. Besides, the morphology of the fractured surface is rough with the dimple, suggesting that the crack directly propagated from the joining interlayer and deflected due to 'TiC nails', thereby forming a dimple-like morphology. Contrarily, in the case of the Cusil- based joint, the degradation of the composite layer is noticeably slower, and the C/SiC layer occupies a significant percentage of the fractured surface, indicating that the C/SiC is strongly bonded to C103. These observations are consistent with the results obtained from SEM analysis. In other words, for ceramic-metal joining, the least amount of degradation of the composite due to the least amount of reactivity between the substrates and the brazing alloy is preferred since it increases the strength of the junction.

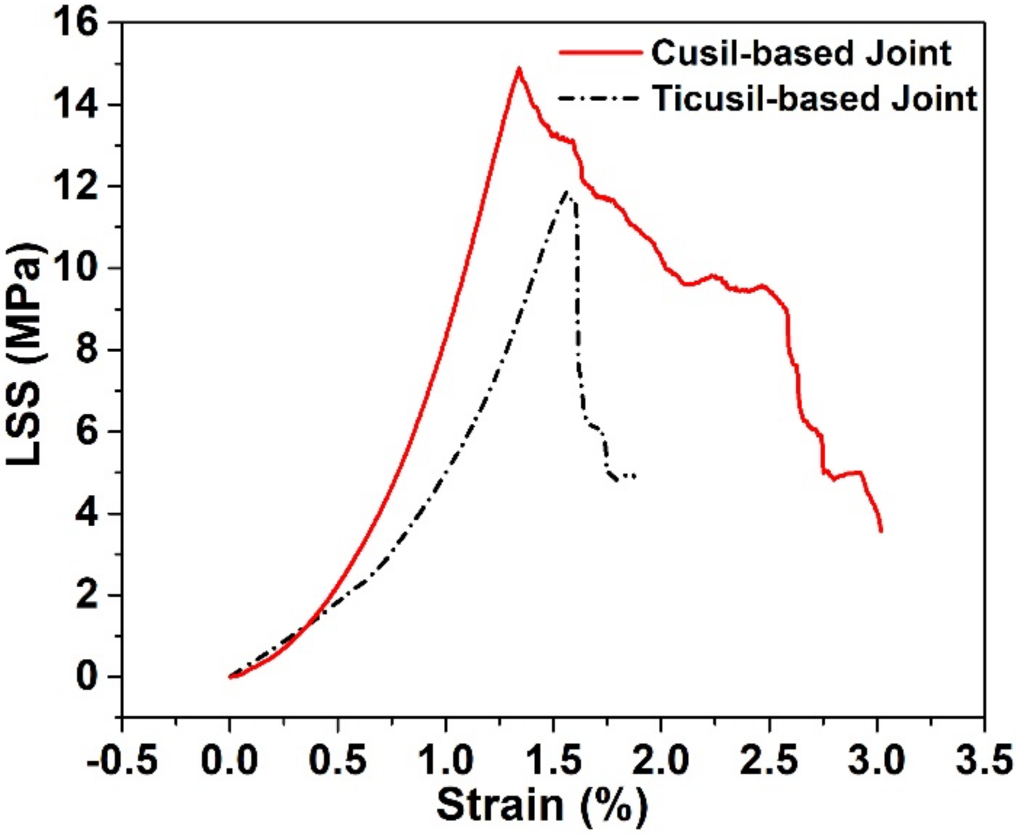

Fig. 4.13: Load-displacement graph of C/SiC-C103 joint.

The load-displacement curve for the LSS evaluation of both joints is depicted in Fig. 4.13. Interestingly, the Ticusil-based joint showed a maximum strain of ~1.5%, whereas the Cusil-based joint showed a maximum strain of ~3%. This indicates that the fracture performance of the Cusil-based joint is superior to that of the Ticusil-based joint. For Cusil-based joints, the LSS-strain curves exhibited a typical ductile-type failure; however, for Ticusil-based joints, failure is seen as an abrupt fracture. The primary cause of the ductile failure of Cusil-based joints is the production of less amount of the brittle phases such as TiC, Nb_2C, and Ti_5Si_3, which serve as crack initiation sites (Fleck et al. 1991, Yang et al. 2017). Therefore, the Cusil-based joint manifests two times higher strain than the Cusil-based joint during failure. In addition, the reaction of Ti with the nearby carbon fibre and SiC matrix degrades the integrity of the C/SiC composite, leading to the penetration of the crack directly through the layer and causing premature failure of the sample (Zhao et al. 2019, Wang et al., 2022a, Wang et al. 2022b). Moreover, the high interface Cu content of the Cusil-based joint led to the relaxation of thermal stresses during cooling, exhibiting ductile behaviour during LSS evaluation (Xiong et al. 2006a).

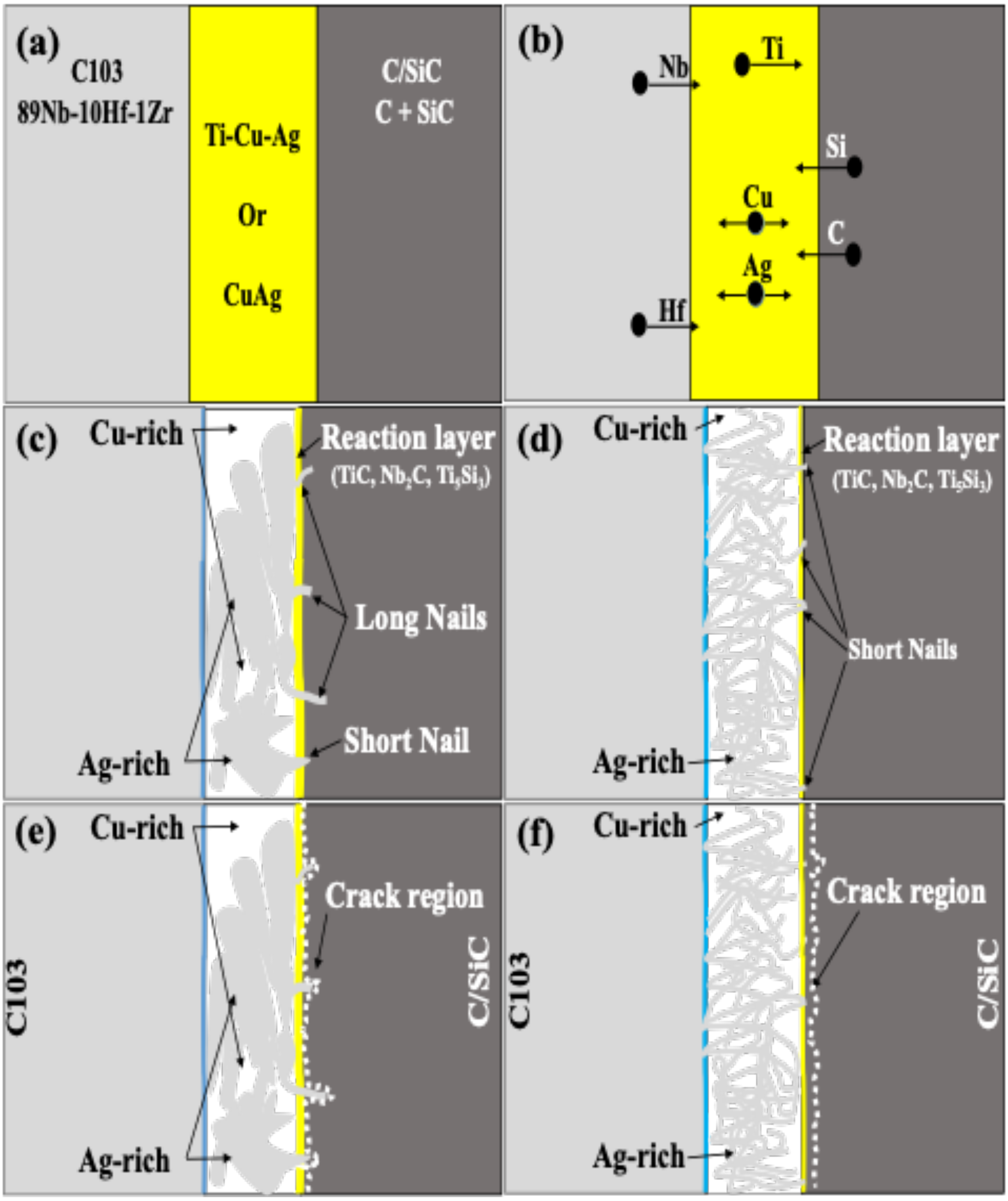

Fig. 4.14: Microstructure evolution mechanism: (a) before joining, (b) during the brazing process, (c) after brazing for Ticusil-based joint, (d) after brazing for Cusil-based joint, (e) during LSS test for Ticusil-based joint, and (f) during LSS test for Cusil-based joint.

4.3.3 Microstructure evolution mechanism

Based on the above discussions, the conceptual phase formation model for the C/SiC–C103 joining process is depicted in Fig. 4.14. The complete microstructure evolution can be divided into four stages. Initially, the C/SiC composites and C103 are sandwiched between the Ticusil or Cusil foil of a thickness of 100 μm (Fig. 4.14a), and the entire assembly is heated to the brazing temperature under vacuum (10^{-3} mbar) with the application of 0.25 kg/cm^2 load. The brazing foil melts, and Ti dissolves into molten braze and diffuses to the C/SiC side. In contrast, Cu and Ag diffuse in either direction towards the substrates. Nb and Hf diffuse in due course to the brazing joint and finally react with the carbon of the C/SiC substrate, as depicted in Fig. 4.14b. As time progressed, an IRZ of thickness ~1–3 μm forms at the interface due to the limited presence of C or SiC species in this region (Fig. 4.14c). In IRZ, the reaction of Ti with SiC forms "nails", and the length of the nails depends on the concentration of Ti. ‘Short nails’ are formed in the Cusil-based joint case (Fig. 4.14d) due to small Ti contents.

Generally, long nails are advantageous as they render good anchoring properties. However, an excess of Ti reduces the homogeneity of the composite and causes premature failure at the interface by forming brittle intermetallic phases (such as TiC, Nb_2C, and Ti_5Si_3). Therefore, an optimum content of Ti in the braze is necessary, which produces metallurgically sound joints with the minimum amount of brittle intermetallics. During loading, the stress is transferred from the brazing joint to the substrates, and then the crack (white-dotted line in Fig. 4.14e and f) is generated at the weaker locations and propagated further in the composite.

4.3.4 RSM analysis and process optimisation

In the present study, temperature (A), reaction time (B), and cooling rate (C) were considered operating parameters that likely affect the LSS of joints. The quadratic function is used to model the LSS. The statistical significance of the quadratic model between temperature, reaction time, and cooling rate was assessed using analysis of variance (ANOVA).

Table 4.6 and Table 4.7 summarise the ANOVA findings for the Ticusil- and Cusil-based joints, respectively. A high R^2-value > 0.9603 and a minimal lack of fit imply that the actual response has significantly less deviation from the predicted response for both joints. As a result, the quadratic model fits the experimental data well with high accuracy. ANOVA results of Ticusil-based joint suggest that the main factors, such as A, B, C, A^2, B^2, and C^2 terms, have a p-value ≤ 0.05, suggesting their contribution is significant, and the contribution of interaction effects such as AB, AC and BC are minimal. The parameters A, and B, the interaction effect between A and B, B and C, and the squared effect of A, B, and C were significant in the case of the Cusil-based joint. The final predicted mathematical models of the LSS for both joints are below:

$$LSS_{Ticusil} = -7518.88 + 18.28A - 0.45B - 9.01C + 0.0007AB + 0.0081AC - 0.00BC - 0.01A^2 - 0.0013B^2 + 0.278C^2 \quad (4.9)$$

$$\mathrm{LSS_{Cusil}} = -1618.2598 + 3.9072\mathrm{A} + 1.2957\mathrm{B} - 4.8055\mathrm{C} - 0.00152\mathrm{AB} + 0.0034\mathrm{AC} - 0.0583\mathrm{BC} - 0.0023\mathrm{A}^2 + 0.0015\mathrm{B}^2 + 0.6534\mathrm{C}^2 \quad (4.10)$$

Table 4.6: Analysis of variance (ANOVA) for LSS response surface quadratic model for Ticusil-based joint

Source	**Sum of Squares**	**df**	**Mean Squares**	**f-value**	**p-value**	**Remark**
Model	196.52	9	21.84	72.73	< 0.0001	Significant
A: Temperature	77.28	1	77.28	257.41	< 0.0001	
B: Time	1.94	1	1.94	6.45	0.0294	
C: Cooling Rate	20.45	1	20.45	68.11	< 0.0001	
AB	0.8450	1	0.8450	2.81	0.1243	
AC	0.8450	1	0.8450	2.81	0.1243	
BC	0.0200	1	0.0200	0.0666	0.8016	
A^2	54.12	1	54.12	180.27	< 0.0001	
B^2	1.92	1	1.92	6.41	0.0298	
C^2	3.41	1	3.41	11.36	0.0071	
Residual	3.00	10	0.3002			
Lack of Fit	2.48	5	0.4965	4.77	0.0557	Not significant
Pure Error	0.5200	5	0.1040			
Total	199.52	19				
Fit Statistics						
Standard Deviation	0.5479	**R^2**	0.9850			
Mean	8.37	**Adjusted R^2**	0.9714			
Coefficient of Variation %	6.54	**Predicted R^2**	0.9206			
PRESS	15.85	**Ad. precision**	31.1078			

Table 4.7: Analysis of variance (ANOVA) for LSS response surface quadratic model for Cusil-based joint

Source	**Sum of Squares**	**df**	**Mean Squares**	**f-value**	**p-value**	**Remark**
Model	116.72	9	12.97	26.90	< 0.0001	Significant
A: Temperature	2.50	1	2.50	5.19	0.0460	
B: Time	2.92	1	2.92	6.05	0.0337	
C: Cooling Rate	0.4410	1	0.4410	0.9148	0.3614	
AB	4.65	1	4.65	9.65	0.0111	
AC	0.1513	1	0.1513	0.3138	0.5877	
BC	67.86	1	67.86	140.77	< 0.0001	
A^2	2.41	1	2.41	5.00	0.0493	
B^2	2.55	1	2.55	5.30	0.0441	
C^2	18.79	1	18.79	38.97	< 0.0001	
Residual	4.82	10	0.4821			
Lack of Fit	3.97	5	0.7935	4.65	0.0585	Not significant
Pure Error	0.8533	5	0.1707			
Total	121.54	19				

Fit Statistics			
Standard Deviation	0.6943	**R^2**	0.9603
Mean	10.18	**Adjusted R^2**	0.9246
Coefficient of Variation %	6.82	**Predicted R^2**	0.7301
PRESS	32.81	**Ad. precision**	17.7611

The process optimisations of the brazing process were performed using the desirability function, and the solution with the highest desirability was considered the optimal solution. The contour plots of LSS desirability for both joints are shown in Fig. 4.15. It can be observed that desirability increases with an increase in temperature for both joints. This is due to the sufficient melting and flowability of the braze material at high temperatures resulting in stronger interfacial bonds. The effect of reaction time on desirability is more pronounced for Cusil-based joints than the Ticusil-based joints. The prolonged reaction time may lead to the formation of inter-metallic Ti_2Cu and $Ti_3(SiCu)C_x$ phases possessing high solidification points and a shortage of liquid phases at the interface due to the ooze-out phenomenon. The high solidification points impede shrinkage of the brazing layer during the cooling process, resulting in pore formation due to insufficient liquid braze to fill the micro-voids (Lin et al. 2007). Such voids are detrimental to the brazed joints, which is possibly why the desirability decreased on higher reaction time for C/SiC–C103 joints.

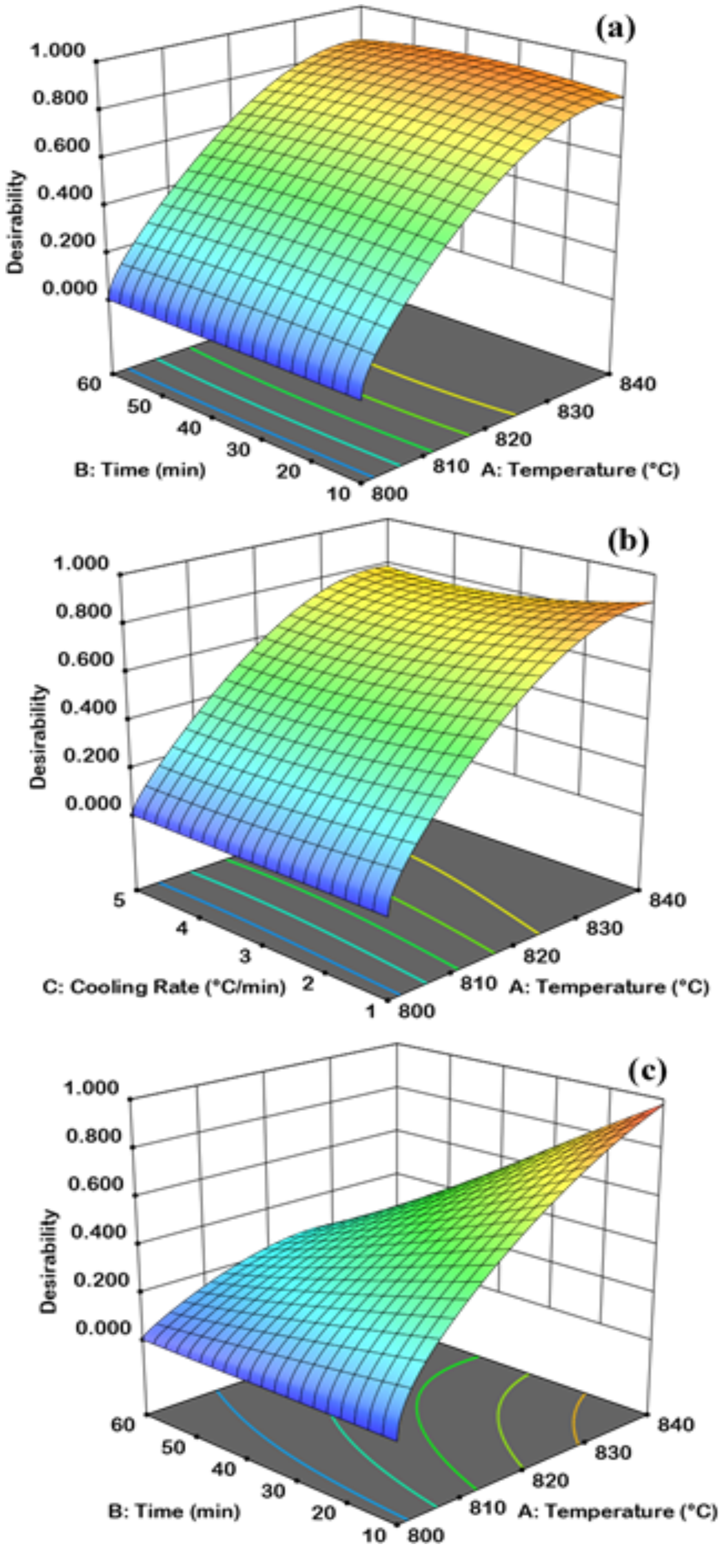

Fig. 4.15: Desirability for (a) and (b) Ticusil-based joint, and (c) Cusil-based joint.

A low cooling rate favoured the high desirability of Ticusil-based joints. Conversely, a high cooling rate is desirable for obtaining high desirability of Cusil-based joints. Further, it is known that the CTE mismatch of the substrates and the intermetallics at the interface produces maximum residual stresses while cooling the joints. In the case of the Ticusil-based joint, a relatively large amount of reaction products (e.g., Nb_2C and TiC, Ti_5Si_3) with thicker IRZ, as discussed above in EDS analysis, are formed due to the high Ti content of the braze material. Because of this, Ticusil-based joints demand a lower cooling rate to accommodate the thermal stresses to obtain a high LSS value. In contrast, the Cusil-based joint witnessed the formation of a low amount of reaction products with thinner IRZ; therefore, the thermal stresses are minimal, and a higher cooling rate is favourable for stronger bonds.

Table 4.8: Optimal process parameters and corresponding LSS for C/SiC–C103 joints

Brazing alloy	**Optimal parameters**			**LSS (MPa)**		
	T (°C)	**t (min)**	**CR (°C/min)**	**Experimental**	**Predicted**	**Relative error**
Ticusil	838	34	1	10.8	11.56	6.57 %
Cusil	840	10	5	15.1	16.14	6.21 %

Table 4.9: Literature reported shear strength of C/SiC- C103 (Nb) joints by brazing process

Filler	**Parameters**	**LSS (MPa)**	**Remarks**	**Ref.**
Ti-Cu	1020°C, 60 min, 0.05-6 MPa	34.1	HP, HT	Xiong 2006a
Ti-Cu	980°C, 30 min, 0.05-8 MPa	14.1	HP, HT	Xiong 2006b
Ticusil	880°C, 10 min, vacuum	NR	HT	Ba 2021
Ti-Cu-Ni-Zr	930°C, 10 min, vacuum	NR	HT	Du 2009
Ti-Ni	1180°C, 20 min, vacuum	NR	HT	Tian 2017
Ti-Ni-Nb	1220ºC, 20 min, vacuum	NR	HT	Liu 2011
Ti-Co-Nb	1280°C, 10min, vacuum	NR	HT	Zhang 2017
Ticusil	838°C, 34 min, vacuum	10.8	-	This work
Cusil	840°C, 10 min, vacuum	15.1	-	This work
HP: High Pressure, HT: High Temperature, NR: Not Reported				

The optimal parameters obtained for both joints are presented in Table 4.8. A comparison of the works carried out for C/SiC to C103 joining by a brazing process is listed in Table 4.9. The high temperature (838°C), intermediate brazing time (34 min), and lower cooling rate (1°C/min) produced the highest LSS value of 12 MPa for the Ticusil-based joint. On the other hand, the high temperature (840°C), lower brazing time (10 min), and higher cooling rate (5°C/min) produced the highest LSS value of 16 MPa for Cusil-based joints. The suggested optimal values of LSS values were validated against the LSS values obtained by performing the experiments under proposed optimal conditions. It was found that the predicted LSS agreed well with the experimental values (relative error < 7%) for both joints.

4.4 Conclusions

C/SiC and niobium alloy (C103) were successfully joined by Ti-containing Cu–Ag highly active and less active filler material using a brazing process. No cracks or voids were found at the C/SiC–C103 interface and the joints were microstructurally sound and fault-free. Depending on the Ti concentration of the Ticusil braze alloy, the joint surfaces of C/SiC–C103 showed a noticeable reaction zone of ~1–3 μm thick titanium carbide near the C/SiC substrate. XRD and EDS suggested the formation of various thermodynamically stable intermediate brittle phases (e.g., TiC, Nb_2C, and Ti_5Si_3) whose concentration is governed by the Ti content of the alloy. The alloy with high Ti content (Ticusil-based joint) formed a thicker brittle reaction layer zone, indicating that the high Ti content of the alloy is beneficial for improving the wettability of the joint. However, it formed large amounts of brittle intermetallics, deteriorating the composite integrity. Therefore, an optimal Ti content of the alloy is necessary to minimise the formation of brittle phases without compromising the joint strength. The RSM-based optimisation study suggested that high temperature (838ºC), intermediate reaction time (34 min), and low cooling rate (1ºC/min) are desirable for obtaining the highest LSS value of 12 MPa for Ticusil-based joint. However, a maximum average LSS value of 16 MPa was reached for the Cusil-based joint when the brazing temperature of 840ºC, a reaction time of 10 min, and a cooling rate of 5ºC/min were maintained. Therefore, the present study suggested that vacuum brazing can successfully join C/SiC to C103 using carefully chosen existing braze alloys to produce mechanically sound joints for space applications.

References:

(1) A. Bartlett, A.G. Evans, M. Rühle, Residual stress cracking of metal/ceramic bonds, Acta Metall. Mater. 39 (1991) 1579–1585, https://doi.org/10.1016/0956-7151 (91)90245-V.

(2) A. Kawecki, T. Knych, E. Sieja-smaga, A. Mamala, P. Kwasniewski, G. Kiesiewicz, B. Smyrak, A. Pacewicz, Fabrication, properties and microstructures of high strength and high conductivity copper-silver wires, Arch. Metall. Mater. 57 (2012) 1261–1270, https://doi.org/10.2478/v10172-012-0141-1.

(3) A.I. Khuri, S. Mukhopadhyay, Response surface methodology, Comput. Stat. 2 (2010) 128–149, https://doi.org/10.1002/wics.73.

(4) B. Cui, J. Huang, C. Cai, S. Chen, X. Zhao, Microstructures and mechanical properties of Cf/SiC composite and TC4 alloy joints brazed with (Ti-Zr-Cu-Ni)+W composite filler materials, Compos. Sci. Technol. 97 (2014) 19–26, https://doi.org/10.1016/j.compscitech.2014.03.021.

(5) C. Liu, J. Chen, H. Han, Y. Wang, Z. Zhang, A long duration and high-reliability liquid apogee engine for satellites, Acta Astronaut. 55 (2004) 401–408, https://doi.org/10.1016/j.actaastro.2004.05.030.

(6) D. Fan, J. Huang, X. Zhao, J. Yang, S. Chen, X. Zhao, Joining of C_f/SiC composite to Ti-6Al-4V with (Ti-Zr-Cu-Ni)+Ti filler based on in-situ alloying concept, Ceram. Int. 43 (2017) 4151–4158, https://doi.org/10.1016/j.ceramint.2016.12.030.

(7) D. Liu, H. Niu, J. Liu, X. Song, L. Xia, J. Feng, Effect of processing parameters on the formation of C_f/LAS composites/Ag-Cu-Ti/TC4 brazed joint, Mater. Char. 120 (2016) 249–256, https://doi.org/10.1016/j.matchar.2016.09.014.

(8) D. Sciti, A. Bellosi, L. Esposito, Bonding of zirconia to superalloy with the active brazing technique, J. Eur. Ceram. Soc. 21 (2001) 45–52, https://doi.org/10.1016/ S0955-2219(00)00162-X.

(9) D.Y. Fan, J.H. Huang, Y.H. Wang, S.H. Chen, X.K. Zhao, Active brazing of carbon fibre reinforced SiC composite and 304 stainless steel with Ti-Zr-Be, Mater. Sci. Eng., A 617 (2014) 66–72, https://doi.org/10.1016/j.msea.2014.08.053.

(10) F.S. Ong, H. Tobe, G. Fujii, E. Sato, Microstructural evolution and mechanical characterisation of Nb-interlayer-inserted Ti–6Al–4V/Si_3N_4 joints brazed with AuNiTi filler, Mater. Sci. Eng., A 778 (2020), 139093, https://doi.org/10.1016/j.msea.2020.139093.

(11) G. Lin, J. Huang, H. Zhang, Joints of carbon fibre-reinforced SiC composites to Ti- alloy brazed by Ag–Cu–Ti short carbon fibre, J. Mater. Process. Technol. 189 (2007) 256–261, https://doi.org/10.1016/j.jmatprotec.2007.01.031.

(12) G.N. Yushin, E.N. Hoffman, A. Nikitin, H. Ye, M.W. Barsoum, Y. Gogotsi, Synthesis of nanoporous carbide-derived carbon by chlorination of titanium silicon carbide, Carbon 43 (2005) 2075–2082, https://doi.org/10.1016/j.carbon.2005.03.014.

(13) H. Yang, X. Zhou, W. Shi, J. Wang, P. Li, F. Chen, Q. Deng, J. Lee, Y.H. Han, F. Huang, L. He, S. Du, Q. Huang, Thickness-dependent phase evolution and bonding strength of SiC ceramics joints with active Ti interlayer, J. Eur. Ceram. Soc. 37 (2017) 1233–1241, https://doi.org/10.1016/j.jeurceramsoc.2016.12.009.

(14) J. Ba, X. Ji, B. Wang, P. Li, J. Lin, J. Qi, J. Cao, Root-like C/SiC surface structure fabricated by the thermal and electrochemical corrosion for brazing to Nb, Compos. B Eng. 218 (2021), 108942, https://doi.org/10.1016/j. compositesb.2021.108942.

(15) J. Ba, X.H. Zheng, R. Ning, J.H. Lin, J.L. Qi, J. Cao, W. Cai, J.C. Feng, C/SiC composite-Ti6Al4V joints brazed with negative thermal expansion ZrP_2WO_{12} nanoparticle reinforced AgCu alloy, J. Eur. Ceram. Soc. 39 (2019) 755–761, https://doi.org/10.1016/j.jeurceramsoc.2018.12.028.

(16) J. Xiong, J. Li, F. Zhang, W. Huang, Joining of 3D C/SiC composites to niobium alloy, Scripta Mater. 55 (2006a) 151–154, https://doi.org/10.1016/j. scriptamat.2006.03.050.

(17) J.M. Shi, L.X. Zhang, X.Y. Pan, X.Y. Tian, J.C. Feng, Microstructure evolution and mechanical property of ZrC-SiC/Ti6Al4V joints brazed using Ti-15Cu-15Ni filler, J. Eur. Ceram. Soc. 38 (2018) 1237–1245, https://doi.org/10.1016/j. jeurceramsoc.2017.11.045.

(18) J.T. Xiong, J.L. Li, F.S. Zhang, W.D. Huang, Joining of 2D C/SiC composites with niobium alloy, Inorg. Mater. 21 (2006b) 1391–1396.

(19) K. Jian, Z.H. Chen, Q.S. Ma, H.F. Hu, W.W. Zheng, Processing and properties of 2D-C_f/SiC composites incorporating SiC fillers, Mater. Sci. Eng., A 408 (2005) 330–335, https://doi.org/10.1016/j.msea.2005.08.205.

(20) K. Zhang, L. Zhang, R. He, K. Wang, K. Wei, B. Zhang, Joining of C_f/SiC ceramic matrix composites: a review, Adv. Mater. Sci. Eng. (2018), 6176054, https://doi. org/10.1155/2018/6176054.

(21) K.K. Chawla, Ceramic matrix materials, in: K.K. Chawla (Ed.), Ceramic Matrix Composites, second ed., Springer US, Boston, 2003, pp. 11–46, https://doi.org/ 10.1007/978-1-4615-1029-1_2.

(22) M. Singh, R. Asthana, Characterisation and control of interfaces for high-quality advanced materials-II, Ceram. Trans. 198 (2007) 9–14.

(23) M. Singh, R. Asthana, T.P. Shpargel, Brazing of ceramic-matrix composites to Ti and Hastealloy using Ni-base metallic glass interlayers, Mater. Sci. Eng., A 498 (2008) 19–30, https://doi.org/10.1016/j.msea.2007.11.150.

(24) M. Singh, T. Matsunaga, H. Lin, R. Asthana, T. Ishikawa, Microstructure and mechanical properties of joints in sintered SiC fibre-bonded ceramics brazed with Ag-Cu-Ti alloy, Mater. Sci. Eng., A 557 (2012) 69–76, https://doi.org/10.1016/j. msea.2012.05.110.

(25) M.C. Halbig, R. Asthana, M. Singh, Diffusion bonding of SiC fibre-bonded ceramics using Ti/Mo and Ti/Cu interlayers, Ceram. Int. 41 (2015) 2140–2149, https://doi. org/10.1016/j.ceramint.2014.10.014.

(26) M.C.L. Patterson, S. He, L.L. Fehrenbacher, J. Hanigofsky, B.D. Reed, Advanced HfC-TaC oxidation resistant composite rocket thruster, Mater. Manuf. Process. 11 (1996) 367–379, https://doi.org/10.1080/10426919608947492.

(27) N.A. Fleck, J.W. Hutchinson, Z. Suo, Crack path selection in a brittle adhesive layer, Int. J. Solid Struct. 27 (1991) 1683–1703, https://doi.org/10.1016/0020- 7683(91)90069-R.

(28) P. Lia, Y. Yan, J. Ba, B. Liu, J. Lin, J. Cao, J. Qi, Design CuZr alloy to control Ti diffusion and reaction layer thickness in C/C-TC4 joins Mater. Char. 188 (2022), 111889, https://doi.org/10.1016/j.matchar.2022.111889.

(29) P. Wang, J. Lin, Z. Xu, B. Qin, J. Cao, J. Feng, J. Qi, Negative thermal expansion of $Sc_2W_3O_{12}$ interlayer with three-dimensional interpenetrating network structure for brazing C/SiC composites and GH3536, Carbon 201 (2023) 765–775, https:// doi.org/10.1016/j.carbon.2022.09.072.

(30) P. Wang, X. Liu, H. Wang, J. Cao, J. Qi, J. Feng, Negative thermal expansion $Y_2Mo_3O_{12}$ particles reinforced AgCuTi composite filler for brazing C_f/SiC and GH3536, Mater. Char. 185 (2022), 111754, https://doi.org/10.1016/j. matchar.2022.111754.

(31) P.D. Awasthi, P. Agrawal, R.S. Haridas, R.S. Mishra, M.T. Stawovy, S. Ohm, A. Imandoust, Mechanical properties and microstructural characteristics of additively manufactured C103 niobium alloy, Mater. Sci. Eng., A 831 (2022), 142183, https://doi.org/10.1016/j.msea.2021.142183.

(32) P.R. Subramanian, D.E. Laughlin, Phase diagrams of binary copper alloys, Monograph series on alloy phase diagrams 10 (1994) 109.

(33) Q. Zhang, L. Sun, Q. Liu, J. Zhang, T. Wang, C. Liu, Effect of brazing parameters on microstructure and mechanical properties of Cf/SiC and Nb-1Zr joints brazed with Ti-

Co-Nb filler alloy, J. Eur. Ceram. Soc. 37 (2017) 931–937, https://doi.org/10.1016/j.jeurceramsoc.2016.09.031.

(34) R.H. Myers, D.C. Montgomery, G.G. Vining, C.M. Borror, S.M. Kowalski, Response surface methodology: a retrospective and literature survey, J. Qual. Technol. 36 (2004) 53–77, https://doi.org/10.1080/00224065.2004.11980252.

(35) S. Kumar, A. Painuly, A. Kamal, S. Kuttappan, R.R. Kumar, P.P. Shyin, R. Devasia, Development of C/SiC fasteners for high-temperature applications, Mater. Perform. Charact. 10 (2021) 253–267, https://doi.org/10.1520/MPC20200161.

(36) S. Schmidt, S. Beyer, H. Knabe, H. Immich, R. Meistring, A. Gessler, Advanced ceramic matrix composite materials for current and future propulsion technology applications, Acta Astronaut. 55 (2004) 409–420, https://doi.org/10.1016/j. actaastro.2004.05.052.

(37) S.B. Lee, J.H. Kim, Finite-element analysis and X-ray measurement of the residual stresses of ceramic/metal joints, J. Mater. Process. Technol. 67 (1997) 167–172, https://doi.org/10.1016/S0924-0136(96)02838-5.

(38) W. Krenkel, Carbon fibre reinforced silicon carbide composites (C/SiC, C/C-SiC), in: N.P. Bansal (Ed.), Handbook of Ceramic Composites, Springer US, New York, 2005, pp. 117–148, https://doi.org/10.1007/0-387-23986-3_6.

(39) W. Wang, Y. Wang, J. Huang, Z. Ye, J. Yang, S. Chen, X. Zhao, Reaction-composite diffusion brazing of C-SiC composite and Ni-based superalloy using mixed (Cu-Ti)+ C powder as an interlayer, J. Mater. Process. Technol. 300 (2022), 117419, https://doi.org/10.1016/j.jmatprotec.2021.117419.

(40) X. Hernandez, C. Jim´enez, K. Mergia, P. Yialouris, S. Messoloras, V. Liedtke, C. Wilhelmi, J. Barcena, An innovative joint structure for brazing Cf/SiC composite to titanium alloy, Mater. Eng. Perform. 23 (2014) 3069–3076, https://doi.org/10.1007/s11665-014-1074-9.

(41) X. Tian, J. Feng, J. Shi, Y. Liu, L. Zhang, Interfacial microstructure and mechanical properties of the vacuum brazed C/SiC composite and Nb joints, Vacuum 146 (2017) 97–105, https://doi.org/10.1016/j.vacuum.2017.09.039.

(42) X. Zhao, L. Duan, Y. Wang, Improved shear strength of SiC-coated 3D C/SiC composite joints with a tailored Ti-Si-C interlayer, J. Eur. Ceram. Soc. 39 (2019) 788–797, https://doi.org/10.1016/j.jeurceramsoc.2018.11.016.

(43) Y. Du, C.Y. Liang, X. Zheng, Joining of Cf/SiC composites with Niobium alloy, Aerosp. Mater. Technol. 39 (2009) 45–48.

(44) Y. Liu, Z.R. Huang, X.J. Liu, Joining of sintered silicon carbide using ternary Ag–Cu–Ti active brazing alloy, Ceram. Int. 35 (2009) 3479–3484, https://doi.org/10.1016/j.ceramint.2009.03.016.

(45) Y. Wang, W. Wang, J. Huang, Z. Ye, J. Yang, S. Chen, Joining of Cf/SiC and stainless steel with (Cu-Ti)+C composite filler to obtain a stress-relieved and high- temperature resistant joint, J. Mater. Res. Technol. 12 (2021) 2026–2041, https://doi.org/10.1016/j.jmrt.2021.04.009.

(46) Y.V. Naidich, V.S. Zhuravlev, I.I. Gab, B.D. Kostyuk, V.P. Krasovskyy, A. A. Adamovskyy, N.Y. Taranets, Liquid metal wettability and advanced ceramic brazing, J. Eur. Ceram. Soc. 28 (2008) 717–728, https://doi.org/10.1016/j.jeurceramsoc.2007.07.021.

(47) Y.Z. Liu, L.X. Zhang, C.B. Liu, Z.W. Yang, H.W. Li, J.C. Feng, Brazing C/SiC composites and Nb with TiNiNb active filler metal, Sci. Technol. Weld. 16 (2011) 193–198, https://doi.org/10.1179/1362171810Y.0000000021.

(48) Z. Wang, H.A. Butt, Q. Ma, Z. Wang, M. Li, Y. Lei, The use of a carbonised phenolic formaldehyde resin coated Ni foam as an interlayer to increase the high- temperature strength of C/C composite-Nb brazed joints, Ceram. Int. 48 (2022) 7584–7592, https://doi.org/10.1016/j.ceramint.2021.11.302.

(49) Z. Yang, L.X. Zhang, X. Tian, Y. Liu, P. He, J. Feng, Interfacial microstructure and mechanical properties of TiAl and C/SiC joint brazed with TiH_2–Ni–B brazing powder, Mater. Char. 79 (2013) 52–59, https://doi.org/10.1016/j. matchar.2013.02.010.

(50) Z. Yang, P. He, L. Zhang, J. Feng, Microstructural evolution and mechanical properties of the joint of TiAl alloys and C/SiC composites vacuum brazed with Ag–Cu filler metal, Mater. Char. 62 (2011) 825–832, https://doi.org/10.1016/j. matchar.2011.05.007.

(51) Z.S. Rak, A Process for C_f/SiC Composites using liquid polymer infiltration, J. Am. Ceram. Soc. 84 (2001) 2235–2239, https://doi.org/10.1111/j.1151-2916.2001.tb00994.x.